The interaction of a coated target and an impinging waterdrop

Gal deBotton

*The Pearlstone Center for Aeronautical Engineering Studies, Department of Mechanical Engineering, Ben-Gurion University of the Negev,
Beer-Sheva 84105, Israel*

Abstract

The work deals with the evolution of the stresses and the damage in targets with thin protective layers due to perpendicular high-velocity waterdrop impacts. The analysis involves a modeling of the impact in the liquid and the solid, and exploration of possible damage mechanisms in the coating and the substrate. We identify three state of stresses that can produce damage, radial tensile stresses that propagate on the surface of the coating, subsurface shear stresses that develop at the coating-substrate interface, and bending stresses near the inner face of the coating. The patterns of these stresses and the locations where they develop are in good agreement with experimental findings. The intensities and the impulses of the stresses are related to the impact velocity by a power-law rule reminiscent of the one used in experimentally motivated damage criteria. We find that the peak of the tensile stresses propagates on the surface of the coating at the speed of the Rayleigh wave in the substrate. The possible role of the subsurface shear stresses in the evolution of damage in coated targets is also discussed.   © 1998 Elsevier Science S.A. All rights reserved.

Keywords: Stresses; Coated target; Waterdrop

1. Introduction

During a high-velocity impact of a liquid-drop on a solid target extremely high pressure develops at the interface between the solid and the liquid. Consequently, for a short instance, intensive stresses that frequently produce local sites of damage develop in the target. Various parameters, such as the duration of the pressure pulse, its magnitude, the mechanical properties of the target and the integrity of its surface, effect the evolution of the damage in the target. If the target is coated with a hard protective layer to improve its resistance to failure, the thickness and the mechanical properties of the layer will influence the evolution of the damage as well. To analyze the impact of a waterdrop on a coated target a model that can account for the effect of these parameters needs to be constructed. Such a model will enable to investigate the transient stress field that develops in the target and, together with available experimental data, to detect the failure mechanisms.

Comprehensive surveys that deal with the problem of liquid-drop impacts onto solid targets, including references to other related works, can be found in the manuscript by Hammitt [1] and in the review article by Lesser [2]. Over the years, various experimental techniques were developed to explore this rapid phenomenon. A jet-gun apparatus for projecting liquid-jets at high velocity was developed by Bowden and Brunton [3] who studied, with the aid of a high-speed photography method, the impacts of the jet on various solid targets. A description of another type of a rain erosion test facility, the whirling-arm, is given in the article by Westmark and Lawless [4], and a list of additional waterdrop impact facilities can be found in Adler [5]. A series of experiments was carried out by Bowden and Field [6], who established the affect of the Rayleigh surface waves on the production of the circumferential fractures around the impact site. Hackworth et al. [7] conducted sequences of single-drops and rainfield experiments with different drop diameters and targets, and measured the damage and loss of transmission of the targets. An estimate for the distribution of the pressure peak across the impact site was determined by Smith and Kinslow [8] from measurements of the pressure during an impact of a liquid-jet on a slip-cast fused silica target. Measurements of the magnitude and the duration the pressure during the impact were also performed by Obara et al. [9] and by Shi et al. [10], who were also able to identify a supersonic shock wave originating from the Rayleigh surface wave. Field et al. [11], Dear and Field [12], and Hand et al. [13] performed a comprehensive sequence of experimental investigations and, with the aid of photos that depict the onset of the jetting stage and the evolution of the damage sites,

examined the significance of the shape of the liquid striker and the target properties. Summaries of experimental studies of water-jet impacts on infrared transmitting composite and coated windows can be found in articles by Van der Zwaag and Field [14], Thomas et al. [15], and Seward et al. [16,17].

Along with the experimental studies analytical investigations were carried out as well. The aim of these studies was two fold, first to characterize the pressure field in the collapsing drop, and second to determine the transient stress field in the solid target and analyze the failure mechanisms. A description of the three principal stages, the compressible stage, the jetting stage and the cavitation stage, that occur during the collapse of a liquid-drop may be found, for example, in Section 5 of Field et al. [11]. Analyses that deal with the pressure build up in the liquid-drop and account for the compressibility of the liquid may be found in the works of Engel [18] and Bowden and Field [6]. Bowden and Field [6] concluded that the pressure at the liquid–solid interface rises to the *water-hammer* pressure

$$P_w = \rho c v \qquad (1)$$

where, ρ and c are, respectively, the density and the sound velocity in water and v is the impact velocity. A refined model that provides an accurate estimate for the pressure near the expanding perimeter of the contact area was introduced by Heymann [19]. Lesser [20] developed an even more comprehensive model that took into account the flexibility of the solid target. All of these analytical models where primarily concerned with the initial high-pressure compressible stage of the impact. Based on experimental observations, ad-hock estimates for the second, jetting stage were proposed by Adler [21] and Field et al. [22].

Various numerical schemes that enabled to determine the temporal and spatial distributions of the pressure and velocity fields during the entire impact event were also constructed. Hwang and Hammitt [23] applied the ComCAM numerical code to study the impacts of cylindrical, spherical and conical drops on rigid targets and obtained predictions for the evolution of the pressure. Johnson [24], studied the impacts of spherical and cylindrical drops by application of the explicit finite element EPIC code where the governing equations are integrated directly. A different numerical scheme was applied by Rosenblatt et al. [25], who determined estimates for the shape of the collapsing drop, the pressure at the liquid–solid interface and its critical size.

A comprehensive analytical study regarding the response of the target was conducted by Blowers [26], who obtained expressions for the transient stress and displacement fields that develop in the solid during the compressible stage of the impact. By application of an analogous method Adler [21] and Hackworth et al. [7] obtained estimates for the stresses that develop in targets that are made of various transparent materials. The WAVE-L numerical code was applied together with analytical estimates for the temporal variations of the stress intensity factor by Evans [27] and Evans et al.

[28] to determined estimates for the impact threshold velocity in terms of the target parameters. By application of the PAFEC code, a quasistatic numerical modeling of the indentation of coated targets by rigid spheres was conducted by Van der Zwaag and Field [29], and the effects of the thickness and the stiffness of the coatings were examined. Adler [30] modeled the impact of a waterdrop on various solid targets by application of the DYNA3D finite element code. In a similar manner Adler and Mihora [31] modeled the impact of a liquid-drop on a transparent window with 0.25 mm thick protective layer.

In this work we study the evolution of the stress and the displacement fields in a coated target during a high-velocity waterdrop impact. The objective is to identify states of stresses that are capable of producing damage in the coating, in the substrate and at the interface between them. A brief summary of the analytical model that is utilized to describe the liquid striker and the finite element model that is used to simulate the solid target is given in Section 2. The results of the simulations of four different impacts of a 2-mm waterdrop on a diamond coated silicon target are described in Section 3. In Section 4, a comparison of the numerical results with experimental and other available data is carried out together with a detailed analysis that identifies the failure mechanisms in the target and the protective layer. Concluding remarks are given in Section 5.

2. Modeling the impact

In this section the model that is utilized to simulate the impact is described in brief. A comprehensive discussion regarding this topic can be found in deBotton [32]. The model is based on the assumption that thanks to the large contrast between the mechanical properties of the drop and the target the pressure field at the liquid–solid interface resembles the one that develops during an impact of a waterdrop on a rigid target. This assumption enables the use of well-established models that describe the pressure field at the liquid–solid interface during an impact of a waterdrop on a rigid target. Consequently, for the solid target, the impact problem can be reformulated as a problem involving a rapid loading whose exact parameters are deduced from these models.

During the collapse of a liquid-drop three predominate stages are distinguished (see, for example, Field et al. [11] and Lesser [2]). The first stage is the *compressible* stage during which the expanding circumferential boundary of the liquid–solid interface moves faster than the speed of sound in water. As a result, the liquid at the impacting edge of the drop is trapped behind the compression wave that propagates into the drop, and the pressure at the liquid–solid interface rises, approximately, to the water hammer pressure. This stage terminates when the velocity of the expanding perimeter reduces below the speed of the compression wave. From geometrical considerations, Bowden and Field [6] showed that the radius of the liquid–solid interface at that instant is

$$R_j = \frac{v}{c} R \qquad (2)$$

and, accordingly, the duration of this stage is [22],

$$T_j = \frac{R_j}{2c} \qquad (3)$$

where R is the radius of the waterdrop. The second, *jetting* stage begins at this time when the compression wave detaches from the solid target and the compressed liquid flows rapidly outwards. In practice, the jetting stage does not begin immediately at this instant but a short time afterwards. The precise time depends on the pattern of the flow near the boundary of the liquid–solid interface and on the stiffness of the target (see discussions in Adler [21] and Field et al. [22]). During the jetting stage a release wave propagates from the circumference towards the center of the impact site and the pressure behind this wave drops to the stagnation pressure. The release time (the time for the release wave to approach the center of the impact site) is $2T_j$ [22] and hence, the total duration of the high-pressure loading cycle is $3T_j$. Finally, during the last stage of the impact, the inward propagating release wave causes cavitation in the liquid-drop.

Following the common notion that the first stage of the impact is the primary source for the damage in the target (see, for example, Kallas [33] and Evans [27]), in this work the contributions of the second and the third stages are neglected. Thus, it is assumed that the interface between the drop and the target has a circular shape whose edge is growing until the jetting stage begins. At this time, while the area of the liquid–solid interface continues to expand, the high-pressure area shrinks at a rate which is approximately equal to the water sonic speed. Additionally, it is assumed that throughout this expanding and shrinking process the pressure of the trapped liquid is uniform and equal to the water-hammer pressure.

The model that is utilized here to describe the transient pressure field in the waterdrop is based on the model of Bowden and Field [6] (see also Refs. [13,22]), and it is evident that it oversimplifies the precise loading sequence. In particular, the nonlinear effect resulting from the fact that the speed of the compression wave depends on the impact velocity is not being accounted for. Thus, during a one-dimensional liquid–solid impact the velocity of the compression wave is $(c + 2v)$ [19] and, accordingly, the pressure at the liquid–solid interface will rise to $P_w(1 + 2v/c)$ [1]. The situation is evidently more complicated when dealing with the impact of waterdrops, and various analytical and numerical estimates for the pressure distribution may be found in the works of Heymann [19], Hwang and Hammitt [23], Rosenblatt et al. [25] and Lesser [20]. On the other hand, we note that for subsonic impacts ($v < 350$ m/s) the duration and the intensity of the pressure pulse, which are the main parameters effecting the damage mechanisms, are similar to those that result from the more comprehensive models of Heymann [19], Hwang and Hammitt [23], Rosenblatt et al. [25] and

Lesser [20]. Moreover, a comparison of the evolution of the average pressure over the impact site as determined by application of this model with corresponding experimental results of Smith and Kinslow [8], Obara et al. [9] and Shi et al. [10], confirms that the estimates for the intensity and the duration of the pressure pulse are reasonably accurate.

The study of the evolution of the stresses in the solid target is accomplished by application of a finite element model. For the axisymmetric problem of a perpendicular impact only a sector of a circular region around the impact site needs to be modeled (see Fig. 1). A detailed discussion regarding the geometry of the finite element model is outside the scope of this work and can be found in deBotton [32]. However, we note that to accurately model the evolution of the stresses, the diameter and the thickness of the specimen (D and h in Fig. 1, respectively) must be large enough so that the stress waves will reflect from the remote boundaries only after the termination of the high-pressure stage. We also note that two distinct length scales emerge in this problem, the diameter of the impacting drop, of order of a few millimeters, and the thickness of the coating, of order of a few microns. The stresses that are associated with Rayleigh surface wave and have an important role in the failure process also appear at the fine scale. The MSC/NASTRAN finite element code that enables to execute dynamic and transient problems was utilized in the 'direct transient response' mode. In this mode direct time integration of the equations of motion, in their matrix form, is performed. Four impacts of 2-mm waterdrops at various speeds on a silicon target with 30 μm protective diamond layer were examined by application of the proposed model. The mechanical properties of the two constituents are summarized in Table 1. The results are summarized in Section 3 and the cylindrical coordinate system that is used to represent the results is shown in Fig. 1.
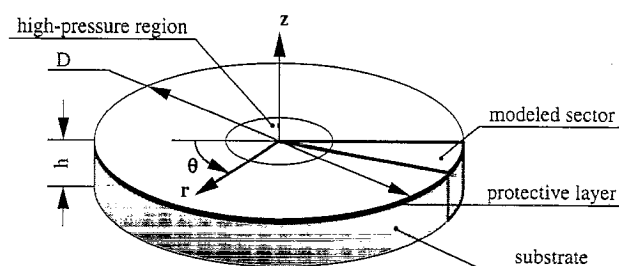

Fig. 1. A circular specimen around the impact site.

Table 1
Physical properties for the two constituents that compose the target

	Silicon	Diamond
Young's modulus (E) [GPa]	110	1150
Poisson's ratio (v)	0.22	0.15
Density (ρ) [kg/m^3]	2330	3510
Dilatational wave speed (c_L) [m/s]	7340	18 600
Distortional wave speed (c_T) [m/s]	4400	11 935
Rayleigh wave speed (c_R) [m/s]	4015	10 710

3. Summary of the results

In this section the response of a coated target to impacts of waterdrops is analyzed. Initially, the evolution of the displacement and the stress fields in a diamond coated silicon target due the impact of a 2-mm waterdrop at 350 m/s are examined. States of stresses that may advance the production of the damage in the target, the coating, and at the interface between them are highlighted. The affect of the impact velocity is investigated afterwards by application of the proposed model to simulate four impacts of 2-mm waterdrops at different velocities. The parameters that characterize the four impacts are listed in Table 2, where T_j, the time to the end of the compressible high-pressure stage and R_j, the radius of the liquid–solid interface at that time are given in Eqs. (3) and (2), respectively.

We emphasize that the loading cycle does not end at T_j but continues until the circumferential release wave approaches the center of the impact site, and thus, the total duration of the loading cycle is $3T_j$. As mentioned before, the above estimates for the impact pressure, its duration and the loading area, are based on the assumption that the velocity of the compression wave is equal to c. This assumption is valid only for relatively low impact velocities and is definitely inappropriate for the 450 m/s impact. Moreover, at high impact velocities it is reasonable to assume that the behavior of the constituents composing the target will be inelastic, and a more general constitutive law will be required (see, for example, the fracture model of Evans et al. [28]). The reasons for the inclusion of the higher impact velocity are to verify whether or not the pattern of the stress distribution changes as the impact velocity increases, and also to check the validity of the various correlation that will be discussed later.

Plots of the axial deflections (u_z, see Fig. 1) of the points at the top surface of the target as functions of their distance from the center of the impact site at various times after the initiation of a 350 m/s impact are shown in Fig. 2. Here, and in the rest of the figures, the distributions during the compressible stage of the impact are plotted with continuous heavy curves, the distributions during the jetting stage with continuous light curves and the post-loading distributions with dashed curves. The vertical line that is labeled R_j shows the location of the perimeter of the contact area between the drop and the target at the end of the high-pressure stage. As expected, the points at the liquid–solid interface moves downwards, and 0.13 μs after the initiation of the impact the maximum deflection of the point at the center of the impact site is 1.85 μm. Interestingly, the point at the center begins to move back upwards before the end of the loading cycle. (According to the applied model the loading cycle ends 0.24 μs ($= 3T_j$) after the initiation of the impact). We also note the outward propagating circular *brim* that rises around the impact site. In fact, in Section 4.1, we demonstrate that this brim corresponds to the Rayleigh surface wave that propagates away from the impact site.

Table 2
Characteristic parameters of the four 2-mm waterdrop impacts that were studied

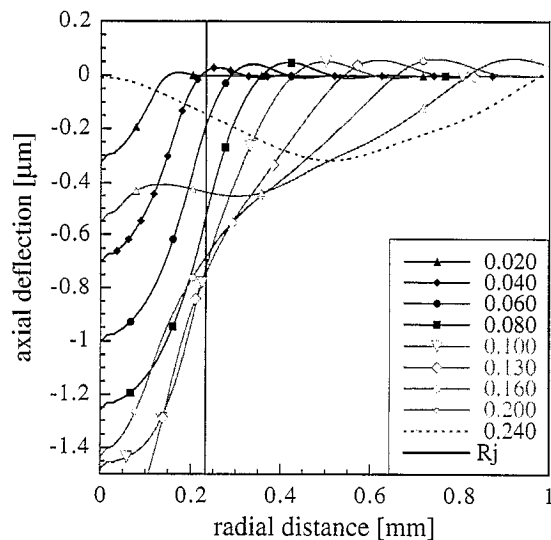|	Impact velocity (m/s)	Water-hammer pressure (MPa)	R_j (μm)	T_j (μs)
1	150	225	100	0.033
2	250	375	167	0.056
3	350	525	233	0.078
4	450	675	300	0.100

Fig. 2. The variation of the axial deflection of the top surface of a 30-μm diamond layer that covers a 1-mm silicon target during an impact of a 2-mm waterdrop at 350 m/s as a function of the distance from the center of the impact site at various times. The time is given in μs.

The distributions of the radial (σ_{rr}), tangential ($\sigma_{\theta\theta}$), axial (σ_{zz}) and inplane shear (σ_{zr}) stresses 5 μm beneath the impacted surface of the protective diamond layer as functions of the distance from the center of the impact site at various times are shown in Fig. 3a through d. The distributions of the radial stresses at the diamond and silicon sides of the interface are shown in Fig. 4. The analogous distributions of the tangential stresses are shown in Fig. 5. The distributions of the axial and the inplane shear stresses at the interface itself are shown in Fig. 6. We recall that since the problem of the perpendicular impact is axisymmetric, there is no deformation in the tangential direction and the out-of-plane shear stress components $\sigma_{r\theta}$ and $\sigma_{\theta z}$ vanish.

In Fig. 3a, that shows the distributions of the radial stresses, we observe that just beneath the high-pressure region the stresses are compressive. The maximal magnitude of these compressive stresses, which is 1800 MPa, is attained during the jetting stage approximately 0.13 μs after the initiation of the impact. We also observe a remarkably high peak of radial *tensile* stresses that develops in the protective layer. In consideration of the crack growth mechanism, which is the predominant failure mechanism in brittle materials, it is reasonable to assume that the contribution of these tensile
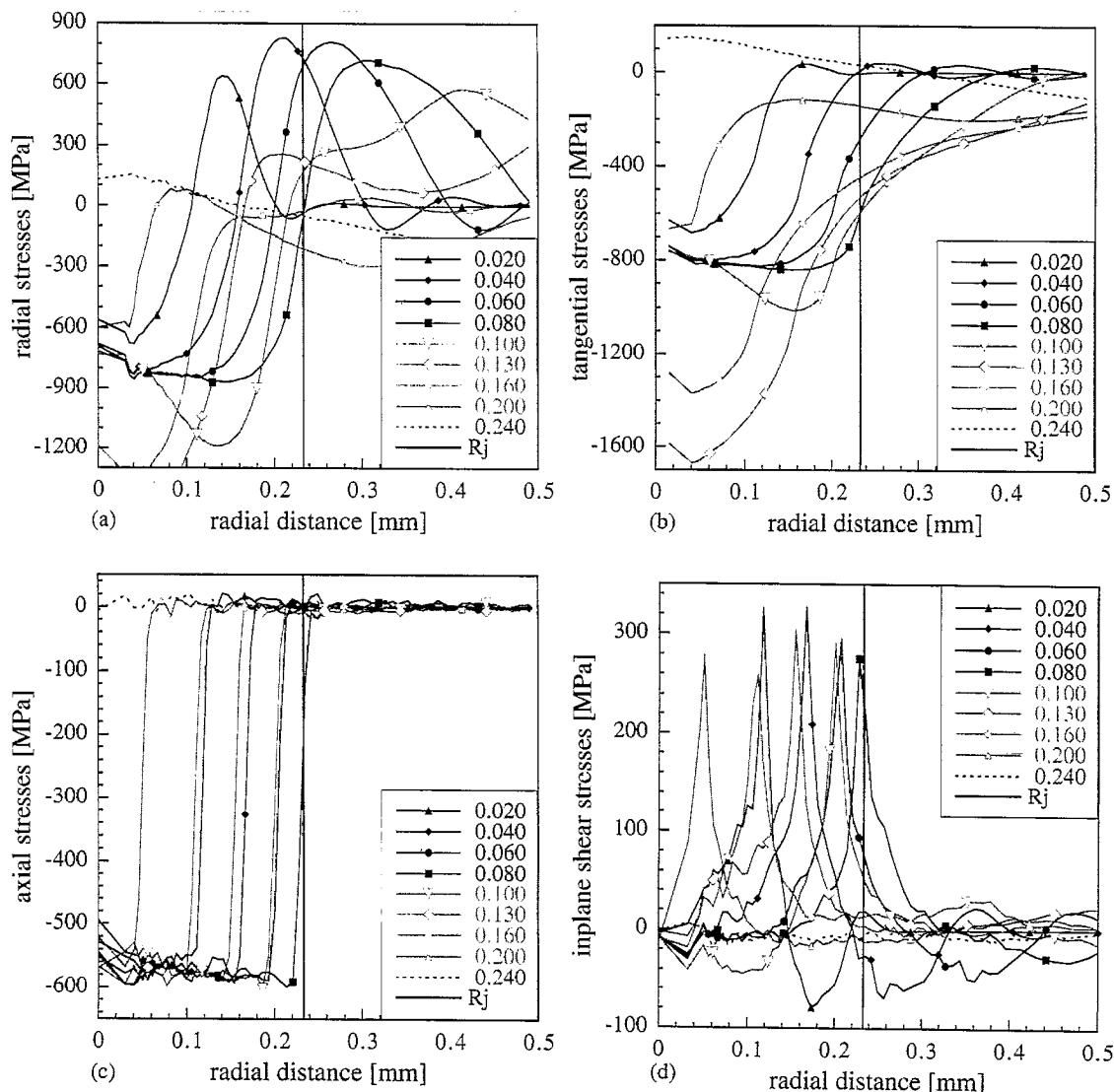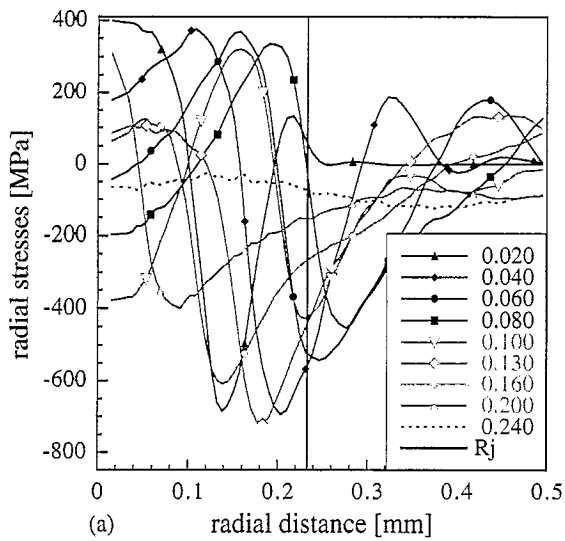
Fig. 3. The distributions of the stresses 5 μm beneath the impacted surface of the diamond coating during an impact of a 2 mm waterdrop at 350 m/s as functions of the distance from the center of the impact site at various times. The time is given in μs.

stresses to the production of the damage is more crucial than that of the compressive stresses. We note that the peak rises during the initial high-pressure stage, attains its maximum value of 845 MPa approximately 0.045 μs after the initiation of the impact, and slowly declines as it propagates outward. In fact, the peak of the tensile stresses accompany the outward propagating brim that was observed in Fig. 2. These findings are in agreement with the results of Blowers [26] who found, in his analytical study of the impact of waterdrops on homogeneous (uncoated) targets, that an intensive peak of radial tensile stresses will develop around the impact site. Rosenblatt et al. [25], who analyzed the problem of waterdrop impacts on homogeneous targets by application of a numerical scheme and assumed pressure distribution at the liquid–solid interface that is different from the one assumed here, also found that a peak of radial tensile stresses will rise around the impact site.

The distributions of the radial stresses on both sides of the diamond–silicon interface are shown in Fig. 4a and b. In Fig.

4a we observe that inside the perimeter of the maximal loading area ($r < R_j$) the radial stresses in the diamond layer are tensile, and attain their maximal value of 400 MPa during the compressible stage. These tensile stresses near the coating–substrate interface develop due to the bending of the protective layer. On the silicon side of the interface (Fig. 4b) the stresses inside the perimeter of the maximal loading area are compressive. The transition from tensile to compressive stresses results because of the combination of high pressure and the fact that the Poisson's ratio of the silicon is larger than that of the diamond. Outside the boundary of the maximal loading area tensile stresses develop both in the coating and the substrate. The magnitude of the maximal tensile stresses in the substrate is approximately 25 MPa, less than one tenth of the corresponding magnitude of the stresses in the protective diamond layer. We note, however, that this reduction in the magnitude of the tensile stresses is smaller than the corresponding reduction in the case of static inden-
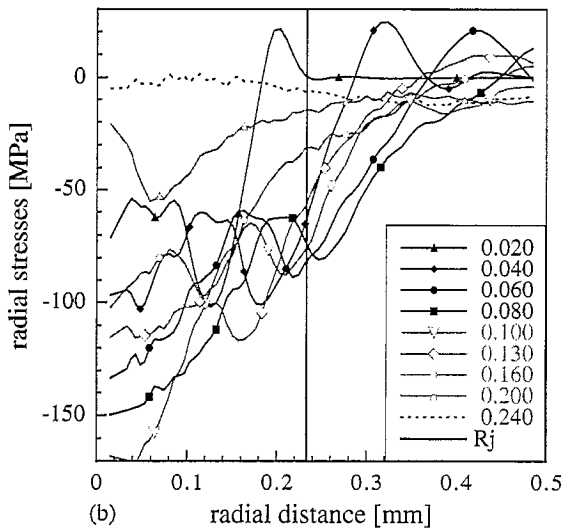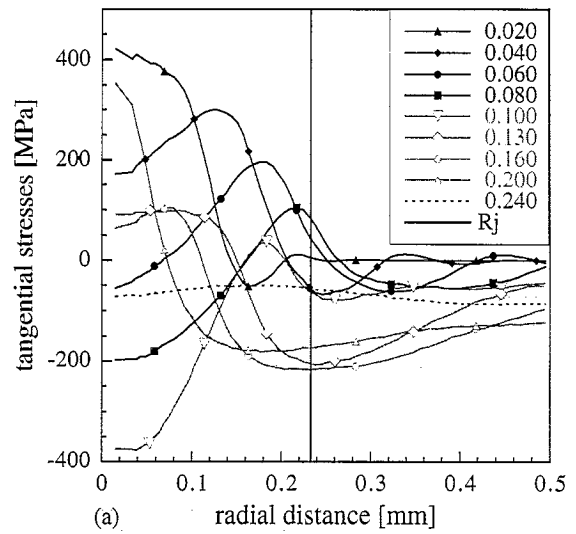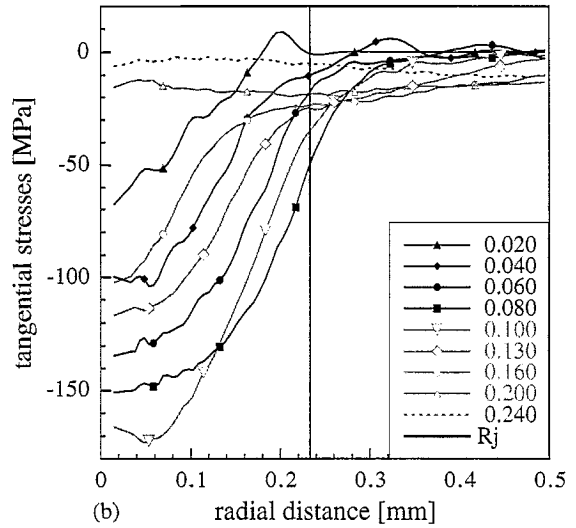
Fig. 4. The distributions of the radial stresses at the diamond side (a) and silicon side (b) of the diamond–silicon interface during an impact of a 2-mm waterdrop at 350 m/s as functions of the distance from the center of the impact site at various times. The time is given in μs.

Fig. 5. The distributions of the tangential stresses at the diamond side (a) and silicon side (b) of the diamond–silicon interface during an impact of a 2-mm waterdrop at 350 m/s as functions of the distance from the center of the impact site at various times. The time is given in μs.

tation of coated targets. Thus, Van der Zwaag and Field [29], found that when the ratio of the Young's moduli of the coating to that of the target is 10, the maximum radial tensile stress in the substrate is less than 1% of the corresponding stress in the target.

Fig. 3b shows the distributions of the tangential stresses in the diamond layer at various times and we observe that these are primarily compressive stresses. Relatively low tensile stresses (approximately 170 MPa) develop at the center of the impact site at the end of the loading cycle 0.23 μs after the initiation of the impact. These are due to the 'springback' of the diamond layer after the release of the load. The distributions of the tangential stresses on both sides of the diamond–silicon interface are shown in Fig. 5a and b. In the vicinity of the interface the distributions of the tangential stresses in the coating and the substrate are reminiscent of the corresponding distributions observed for the radial stresses.

Once again, we note that the stresses in the substrate, in particular the tensile stresses, are considerably lower than the stresses in the protective layer.

Fig. 3c shows the distributions of the axial stresses 5 μm beneath the impacted surface of the diamond layer, the stresses are compressive. The circumference of the compressed region agrees with the instantaneous perimeter of the liquid–solid interface and it expands and shrinks during the compressible and the jetting stages, respectively. The corresponding stress distributions at the diamond–silicon interface are shown in Fig. 6a. In contrast with the previous results for the radial and the tangential stresses, here, there is only a moderate decrease in the magnitude of the stresses and their distributions resemble the corresponding distributions beneath the impacted surface of the diamond layer.

Fig. 3d shows the distributions of the inplane shear stresses in the vicinity of the impacted surface. The corresponding
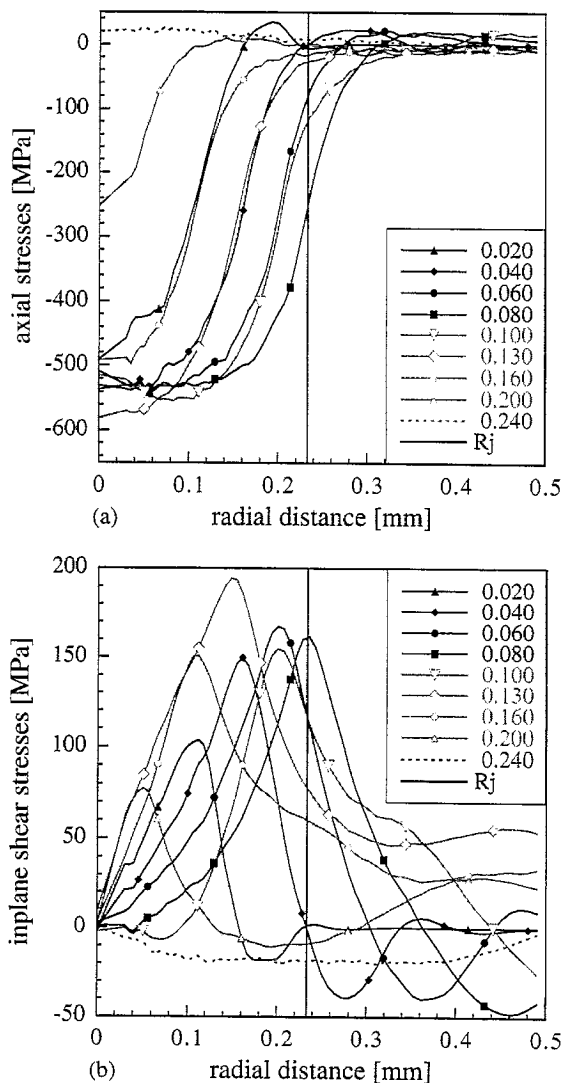
Fig. 6. The distributions of the axial stress (a) and the inplane shear stress (b) at the diamond–silicon interface during an impact of a 2-mm waterdrop at 350 m/s as functions of the distance from the center of the impact site at various times. The time is given in μs.

distributions at the diamond–silicon interface are shown in Fig. 6b. We observe the rise of a peak of shear stresses that follows the perimeter of the loaded area to values of 300 MPa in the diamond layer and 200 MPa at the coating–substrate interface. We note that the peak of the shear stresses does not decay during the pressure release stage. This probably results from the fact that in the present model it was assumed that during the jetting stage the pressure behind the release wave is zero. This assumption oversimplifies the actual state of the pressure existing in the collapsing waterdrop, and it is reasonable to assume that the release of the high-pressure is gradual (see, for example, Hammitt [1], Rosenblatt et al. [25] and Field et al. [22]). We also note that, in passing from the diamond layer to the substrate, the reduction in the magnitude of the shear stresses is not noticeable as the reduction observed for the radial and the tangential stresses.

It is evident that throughout the impact event the highest stresses develop near the top boundary, primarily in the dia-

mond layer. A comprehensive discussion concerning the associated failure mechanisms in the vicinity of this boundary will be carried out in Section 4. However, it is worth nothing that high stresses also develop inside the substrate far from the impact site and the protective layer. Discussions that highlight these remote locations and provide estimates for the stresses and the damage that develop there may be found in the works of Bowden and Field [6], Obara et al. [9] and deBotton [34].

The response of a 1-mm silicon target with a 30-μm protective diamond layer to impacts of 2-mm waterdrops at 150, 250 and 450 m/s was also examined (see Table 2). It was found that the evolution of the stress and the displacement fields were analogous to those determined for the 350 m/s impact. Clearly, the magnitudes of the stresses and the displacements due to these impacts are different, but the tendencies are identical. Thus, in all the cases we considered, the radial stresses beneath the high-pressure domain where compressive and an outward propagating peak of radial tensile stresses was observed. At the impacted surface of the coating the tangential and the axial stresses where mainly compressive and a peak of intensive inplane shear stresses that follows the instantaneous circumference of the high-pressure region was detected. At the diamond–silicon interface radial and tangential tensile stresses develop in the coating due to its bending.

4. Mechanisms of failure

The aim of this section is to characterize and analyze the failure mechanisms in coated targets by linking the estimates that were obtained for the stress field with corresponding data that is available in the literature. In the process of analyzing the evolution of the damage it is important to note that the target is made up of two brittle constituents. In these materials the predominant failure mechanism is crack growth, and hence, it is more likely that damage will develop due to tensile or shear loads and not because of compressive loads (see, for example, Evans et al. [28]). In view of the findings in Section 3, the stresses that are most likely to produce damage in the target are the radial tensile stresses that develop in the diamond layer, the subsurface inplane shear stresses that develop beneath the perimeter of the high-pressure domain, and the bending stresses that develop near the coating–substrate interface. Accordingly, in this section, we will focus on revealing the relationships between known failure mechanisms in impacted targets and these states of stresses.

4.1. The Rayleigh surface wave

Bowden and Field [6] demonstrated that the circumferential cracks around the impact site are produced by the Rayleigh surface wave. The confirmation of this conjecture was based on the realization that in some cases a secondary ring of damage, with radius that is larger than the radius of the

primary ring, is produced. A comparison between the radius of the secondary ring with the theoretical prediction for the location where the body stress-waves that reflect from the rear surface will reinforce the Rayleigh wave at the front surface revealed remarkable agreement (Fig. 14 ibid.).

Motivated by this experimentally verified observation for *uncoated* targets, we examine the rate of the propagation of the peak of the radial tensile stresses that accompany the outward expanding brim around the impact site. Fig. 7 shows the distance of the peak of the radial tensile stresses from the center of the impact site as a function of the time elapsed from the initiation of the impact. We observe that the rate of the propagation of the stress peak is constant. Further, the slops of the curves for the numerical results agree with the slop of the thick continuous (unmarked) curve that corresponds to the theoretical speed of the Rayleigh wave in the *silicon* substrate (4015 m/s). We can conclude that, in a manner similar to the one observed for uncoated targets, the stresses that are associated with the Rayleigh wave may produce circumferential ring of fractures in coated targets as well. Oddly however, while these surface waves propagate on the surface of the diamond coating, their velocity is equal to the velocity of the Rayleigh wave in the substrate. This can have a considerable effect on the development of secondary rings of fractures in coated thin targets since the velocity of the surface waves in the substrate is lower than that of the surface wave in the coating material. Thus, in thin targets the dilatational stress waves that reflect from the rear surface of the target will reinforce the Rayleigh waves near the impact site, whereas, if the surface waves would have propagate at the speed of the Rayleigh wave in diamond (10710 m/s) the slower body stress waves in the silicon substrate would have never caught up with them.

4.2. The variation of the loading with the impact velocity

At the end of Section 3 we concluded that the spatial distributions of the stresses during the four impacts are reminiscent while the magnitudes of the stresses strongly depend on the velocity of the collision. This observation suggests that a firm correlation between the maximal stress that is attained during the impacts and the impacts velocities can provide an insight about the variation of the stress field with respect to the impact velocity. In fact, Rosenblatt et al. [25] found that, during a 222 and 341 m/s impacts of 2-mm waterdrops on a zinc-selenide target the maximal radial tensile stresses at a depth of 12.5 µm beneath the surface are proportional to the square of the impact velocity. The analytical results of Hackworth et al. [7] (Table 5) for 222 and 341 m/s waterdrop impacts on various homogeneous targets suggest that such correlation can be used to obtain first order approximation to the maximal radial tensile stresses beneath the surface. Certainly, it is of interest to verify if a similar correlation is also adequate for the stresses that develop in coated targets.

Fig. 8 shows the maximal radial tensile stresses that develop 5 µm beneath the surface of the diamond coating
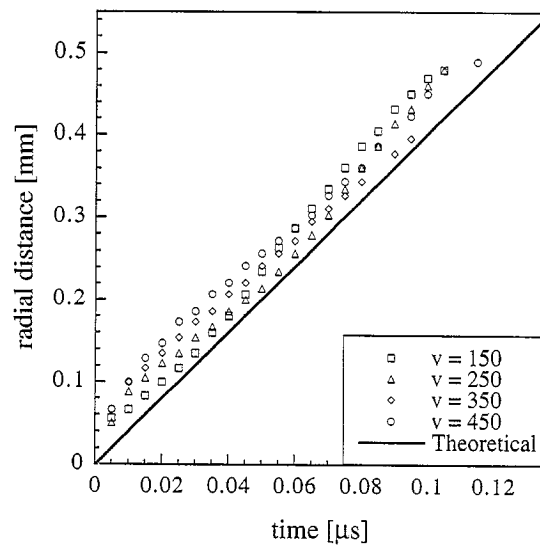

Fig. 7. The distance of the peak of the radial stresses from the center of the impact site as a function of the time elapsed from the initiation of an impact of a 2-mm waterdrop on a silicon target coated with a 30-µm diamond layer. The markers correspond to different impact velocities and the slop of the thick curve is equal to the speed of the Rayleigh wave in silicon. The velocities are given in m/s.
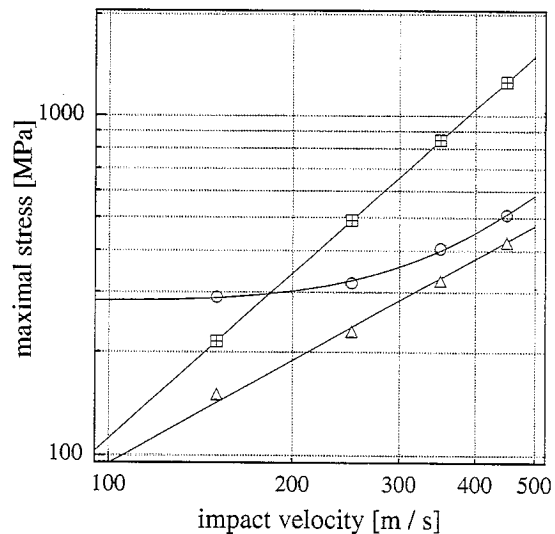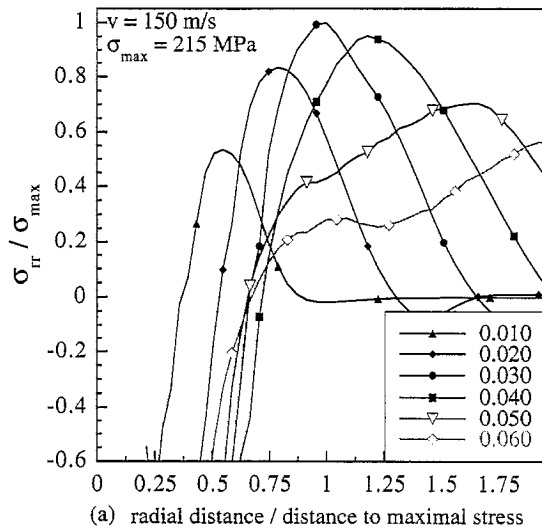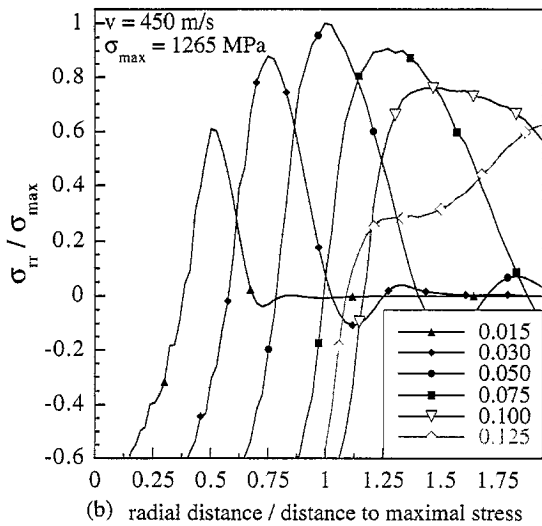

Fig. 8. The dependence of the maximal stresses on the impact velocity. The squares, the circles and the triangles correspond to the radial tensile stresses 5 µm beneath the surface of a diamond coated silicon target, the radial tensile stresses at the diamond–silicon interface, and the inplane shear stresses in the coating, respectively. The corresponding curves are linear and quadratic best curve fits.

(squares), the maximal radial tensile stresses that develop at the diamond side of the diamond–silicon interface (circles), and the maximal inplane shear stresses in the coating (triangles) as functions of the impact velocity. The marks for the maximal radial tensile stresses at the surface are aligned along a straight line whose slope on a logarithmic scale is 1.61. This suggests that the radial stresses at the surface are proportional to the impact velocity raised to the 1.61 power. The plots in Fig. 9, that shows the distributions of the radial stresses at the surface of the coating during 150 and 450 m/s

Fig. 9. The distribution of the radial stresses 5 μm beneath the surface of the diamond coating normalized by the maximal stress vs. the distance from the center of the impact site normalized by the distance to the maximal stress during 150 and 450 m/s impacts. The time is given in μs.

impacts, demonstrate that indeed such a correlation can be used to obtain first order estimates for the Rayleigh stresses as functions of the impact velocity. It should be noted however that the correlation exponent possibly depends on the elastic properties of the target.

We also observe in Fig. 8 that the maximal subsurface shear stresses grows linearly with the impact velocity, and thus, are proportional to the water-hammer pressure. The marks for the radial tensile stresses that develop at the diamond–silicon interface due to the bending are not aligned along a straight line, however, at impact velocities above 170 m/s these stresses are lower than the tensile stresses at the impacted surface.

We note that under rapid loading conditions, when the duration of the impact is shorter than the characteristic response time of the target, the damage mechanism is often proportional to the impulse of the load and not merely to its intensity. This observation suggests that the variation of the
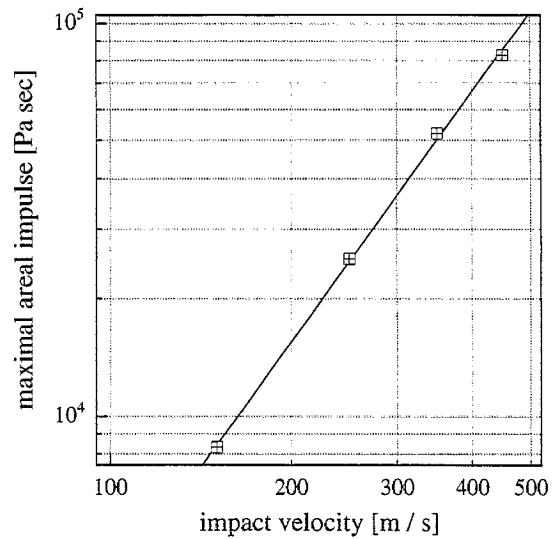

Fig. 10. The maximal impulse of the radial tensile stresses 5 μs beneath the surface of the diamond coating as a function of the impact velocity.

impulse of the radial tensile stresses in the diamond layer as a function of the impact velocity should be examined. The areal impulse of the radial tensile stress, namely,

$$I(r,z) = \int_{t_1}^{t_2} \sigma_{rr}(r,z,t)\,\mathrm{d}t \tag{5}$$

was determined 5 μm beneath the surface as a function of the distance from the center of the impact site. The numerical integration was performed in the time interval between t_1 and t_2 such that during this time $\sigma_{rr}(r,z,t) > 0$. The maximal impulse of the radial tensile stresses as a function of the impact velocity is shown in Fig. 10, and it is important to note that the maximal impulse is not attained at the same point where the maximal stress is attained. On a logarithmic scale the marks are aligned along a straight line, implying that the maximal areal impulse of the Rayleigh stresses is proportional to the impact velocity raised to the 2.11 power.

On grounds of a sequence of experiments, Hand et al. [13] concluded that for uncoated targets the failure criterion

$$\sigma_n^2 T \leq K_o \tag{4}$$

where σ_n is a stress pulse, T is the duration of the pulse and K_o is a material constant, applies reasonably well to waterdrop impacts on brittle targets by letting σ_n be equal to the water-hammer pressure P_w. From Eqs. (1)–(3) it follows that the term on the left hand side of inequality (Eq. (4)) is proportional to v^3. We note that in comparison with the correlation found for the maximum of the tensile stresses at the surface, the one for their maximal impulse is in better agreement with this experimentally verified failure criterion. Clearly, a finer model for the evolution of the pressure in the waterdrop, one that will incorporate the nonlinear growth of the pressure with the impact velocity, will lead to a steeper dependence of the stresses on the impact velocity and consequently to a better agreement with the experimental criterion.
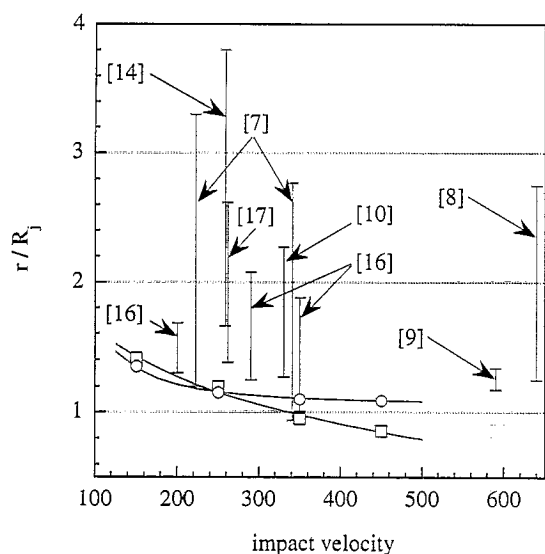
Fig. 11. Inner and outer radii of the ring of fractures according to various sources (the numbers in brackets correspond to the numbers in the references list), and the location of the points where the maximal radial tensile stresses (squares) and their impulse (circles) were attained 5 μm beneath the surface of the coating. The distances are normalized by the radius of jetting or its equivalent.

4.3. The pattern of the damage

In brittle targets the pattern of the surface damage due to waterdrop impacts is in the form of a ring of fractures around the impact site. In ductile targets, where the primary failure mechanism is plastic flow, the damage appears in the form of a circular crater around the impact site. In spite of the fact that the damage mechanisms are different in these two cases, the spatial distributions of the damage sites are reminiscent. This observation suggests that the same state of stresses initiates the damage in both types of materials and motivates a comparison of the estimates for the stresses with corresponding photographs of impacted targets.

Photographs that where taken during impacts of water-jets on various targets and photographs of damaged sites after the impact can be found in the literature. It should be noted that usually these photographs correspond to impacts of water-jets and not waterdrops. However, there is a close analogy between the two cases, and for a given impact velocity, a correlation between a water-jet diameter and a waterdrop diameter that produce the same damage can be found (see, for example, Hand et al. [13]). Thus, the pattern of the damage produced by these two, geometrically different, strikers is almost identical and we may regard the impact sites produced by water-jets as if produced by waterdrops with appropriate 'equivalent' diameter.

The damage to two slip-cast fused silica specimens due to impacts of 2.4 mm (0.094 in) water-jets at 640 m/s is shown in Fig. 6 of Smith and Kinslow [8]. Fig. 5 of the same reference shows the cross sections of the craters that were formed due to the impacts, the diameters of the inner and outer boundaries of the circular craters are, respectively, 3.2

and 7.0 mm. Waterdrops impacts on PMMA and zinc-selenide targets were examined by Hackworth et al. [7]. The radial distances of the circumferential fractures from the center of the impact site were summarized in Fig. 2 of that article. For 2-mm waterdrop impacts on zinc-selenide targets the inner and the outer radii of the ring of fractures were respectively 0.175 and 0.49 mm for the 222 m/s impact and 0.215 and 0.635 mm for the 341 m/s impact. Fig. 3 in the work of Van der Zwaag and Field [14] includes photographs of impacted sites on 3-μm carbon coated germanium targets after collisions with 0.8 mm water-jet at 260 m/s. In Fig. 3a ibid., the diameter of the inner ring of the circumferential cracks around the impact site is 1.40 mm and the outer diameter is 3.2 mm. The damage to the surface of a 1-μm nanophase diamond coating on a zinc-sulfide substrate due to an impact of a 0.8 mm water-jet at 290 m/s is shown in Fig. 5 of Seward et al. [16]. The inner and the outer diameters of the circumferential fractures are 1.08 and 1.8 mm, respectively. In the same article the damage to composite zinc-sulfide target with 20% diamond particle due to water-jets impacts at 200 and 350 m/s is also shown. The inner diameters of the damaged rings are 1.1 and 0.9 mm for the 200 and the 350 m/s impacts, respectively, and the corresponding outer diameters are 1.41 and 1.67 mm. Sequences of photographs that were taken during the impact of a 3 mm water-jet at 590 m/s on a PMMA target are shown in the work of Obara et al. [9]. The first frame in Fig. 5 of that work was taken 0.6 μs after the initiation of the impact. The opening of cracks on the surface of the PMMA specimen can be observed and the diameter of the forming ring of cracks is approximately 3.8 mm. The damage to a PMMA specimen due to five impacts of a 2-mm water-jet at 329 m/s is depicted in Fig. 6 of Shi et al. [10]. The diameter of the inner circumference of the ring of cracks is, approximately, 2.8 mm and the corresponding outer boundary is 5.0 mm. Finally, we also examine Fig. 5a from the work of Seward et al. [17] that shows the damage to the surface of a germanium target with 16.2 μm boron phosphide coating after 200 impacts of a 0.8 mm water-jet at 260 m/s. The inner and outer diameters of the ring of circumferential fractures are, respectively, 1.15 and 2.2 mm.

The inner and outer radii of the circumferential damage, normalized by R_j, the radius of the liquid–solid interface at the instant when the jetting stage begins, are shown in Fig. 11. For the water-jet impacts an equivalent radius was determined by application of the correlation proposed by Hand et al. [13]. This equivalent radius is usually a few percentages larger than the radius of the water-jet itself. The radii where the maximal radial tensile stresses (squares) and their impulses (circles) were attained according to the numerical model are also shown in the figure. At impact velocities lower than 300 m/s the curves for the maximal stresses and impulses are close, and both agree with the inner radii of the circumferential damage. At higher impact velocities, the peak of the tensile stresses is attained inside the maximal high-pressure domain. At these velocities the point where the maximal impulse is attained is at a distance which is larger than
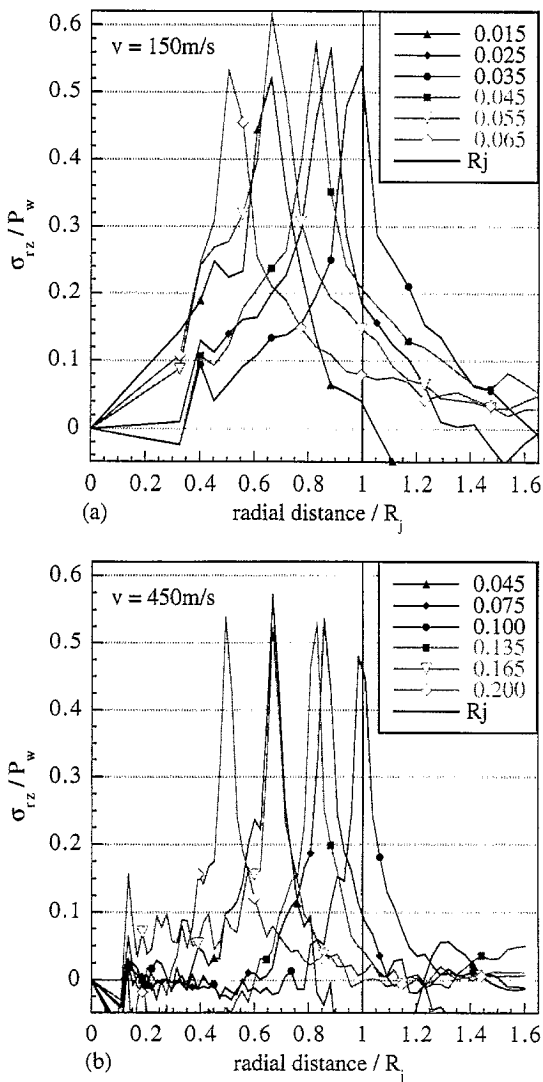
Fig. 12. The distributions of the inplane shear stresses normalized by the water-hammer pressure vs. the radial distance from the center of the impact site normalized by the maximal radius of the high-pressure area during 150 and 450 m/s impacts. The time is given in μs.

R_j and closer to the point where the circumferential cracks originate.

4.4. The inplane shear stresses and their role

The distributions of the inplane shear stresses at various instants during the 150 and 450 m/s collisions as functions of the distance from the center of the impact site, normalized by the maximal radius of the high-pressure area, are shown in Fig. 12. The stresses are normalized by the water-hammer pressure. We observe that the intensity and the pattern of the normalized shear stresses are almost identical during the two impacts, implying that the inplane shear stresses are proportional to the pressure at the liquid–solid interface. Analogous plots for the evolution of the inplane shear stresses during the 250 and 350 m/s impacts where found to be comparable with the plots in Fig. 12.
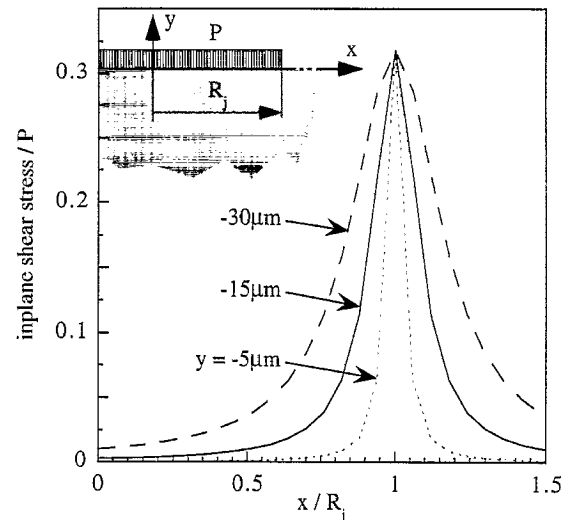

Fig. 13. The distribution of the inplane shear stress as a function of the distance from the origin due to the application of a uniform pressure load in the interval $(-\infty < x \leq R_j]$ on an infinite halfspace. The shear stress is normalized by the applied pressure and the distance from the origin is normalized by the distance of the point where the load terminates. The dotted, continuous and dashed curves correspond, respectively, to the distributions of the inplane shear stress 5, 15 and 30 μm beneath the surface.

The fact that the inplane shear stresses are proportional to the applied load motivates a comparison of the time dependent results with corresponding static, or possibly, quasistatic estimates. The reason being that within the static formulation (with linear elastic materials) the induced stress field is exactly proportional to the applied load. To make this comparison simple and authentic the following observation is useful. Thus, we note that stress-waves in diamond are approximately 10 times faster than the stress-waves in water. This suggests that during the termination of the high-pressure stage, when the velocity of the boundary of the high-pressure domain (see Fig. 1) is lowest and equal to the sound velocity in water, the state of the stresses few tenths micrometers around the edge of the high-pressure region resembles the state of the stresses in an infinite half space subjected to uniform pressure on part of its boundary. An illustration of the relevant quasistatic idealization is shown in Fig. 13, where, the distance from the origin to the point where the load terminates ($R_j = 167$ μm) was chosen to match the maximal radius of the high-pressure domain during an impact of a 2-mm waterdrop at 250 m/s.

Fig. 13 shows the distributions of the inplane shear stress as functions of the distance from the origin at different depths (5, 15 and 30 μm) due to a constant (in time and space) pressure load that is applied to the surface of an infinite halfspace from a given point to negative infinity (see, for example, Section 4 of Timoshenko and Goodier [35]). The shear stresses are normalized by the applied pressure and the distances are normalized by the distance from the origin to the point where the load terminates. We observe that a peak of shear stresses emerges just beneath the point where the load terminates. The magnitude of the peak is constant

(P/π) but, the important observation is that the width of the peak approaches zero near the top boundary. We also note that Van der Zwaag and Field [29], in their investigation of the static indentation of coated targets, also found that a peak of inplane shear stresses will rise at the coating–substrate interface immediately around the contact zone.

A comparison of the quasistatic results with the corresponding results of the full dynamic analysis (Fig. 12), reveals that both analyses predict the existence of an intensive peak of inplane shear stresses just beneath the point where the load terminates. The magnitudes of the loads are of similar order (approximately 0.55 of the applied load in the dynamic configuration and 0.32 of the applied load in the quasistatic configuration). The width of the peak in the dynamic analysis is also comparable with the width of the peak in the static analysis.

We note that since the width of the peak of the shear stresses approaches zero near the top boundary, when this peak travels outward together with the edge of the high-pressure region, the time interval during which a point near the surface is exposed to the high shear stresses is shorter than the incubation time required for cracks opening. In fact, at the top boundary the shear stress must be equal to zero in order to match the boundary conditions.

If we pursue the analogy between the static and the dynamic configurations a little further, we note that according to the static analysis the time period during which points away from the surface are exposed to high shear stresses is longer than the corresponding time to which points near the surface are exposed to these loads. This means that failures due to the shear stresses will probably initiate *beneath* the surface, where the impulse of the shear loads is stronger. In homogeneous materials, however, the density of the surface flaws is usually larger than the density of the flaws inside the body. Accordingly, it is expected that in homogeneous targets, the failure mechanism that is associated with the radial tensile stresses at the impacted surface will be the favorable failure mechanism. Nevertheless, it is known that subsurface failures do appear under certain circumstances (see, for example, Westmark and Lawless [4]).

The situation is different with coated targets. In these targets the shear stresses couple with the preexisting thermal residual tensile stresses, that develop in the substrate during the cool down stage of the manufacturing process, to accelerate subsurface failures. Additionally, various imperfections, such as local separation of the coating, may preexist at the interface between the substrate and the protective layer. Roughly, we can approximate these imperfections as small penny shaped cracks that are aligned with the surface of the interface. The stress intensity factor for such cracks inside the solid is almost identical to the corresponding stress intensity factor for semi-circular surface cracks (see, for example, Tada et al. [36] for the former, and Raju and Newman [37] for the latter). This suggests that, in coated targets, the subsurface mechanism that is associated with the shear loads may produce damage at impact velocities that are lower than

the failure mechanism that is associated with the radial stresses. The reason being that the shear stresses develop in the substrate and at the interface, whereas, the radial stresses develop in the much tougher protective layer. The damage anticipated from such a subsurface failure mechanism is debonding or striping of the protective layer from the substrate (see, for example, Fig. 3 of Van der Zwaag and Field [14] and Section 3.2 of Seward et al. [16]).

5. Concluding remarks

A model for analyzing high-velocity impacts of waterdrops on targets with protective coatings was constructed. The characterization of the pressure field in the waterdrop was based on an analytical formulation, and the analysis of the evolution of the stresses in the target was accomplished with a finite element model. This combined model enabled to simulate various drops parameters in a straightforward manner. Application of the model to the study of four waterdrop impacts on a diamond coated silicon target indicated that while the magnitudes of the stresses that develop during the various impacts are different, the spatial and temporal distributions of the stress fields are essentially the same.

Three primary state of stresses that may produce damage were identified, the radial tensile stresses that propagate outwards on the surface of the coating, the shear stresses that develop beneath the instantaneous circumference of the high-pressure domain, and the radial and tangential tensile stresses that develop in the coating due to its bending. It was found that the peak of the radial tensile stresses that propagate on the surface of the coating travels at a speed which is equivalent to the speed of the Rayleigh wave in the substrate. Correlations that enable to estimate the magnitude of the radial tensile stresses and their impulse in terms of the impact velocity were proposed. Comparison with various experimental photographs that depict impacted sites demonstrated that fair agreement exists between the pattern of the damage and the state of the radial tensile stresses that was determined by the model. Damage patterns that are related to the inplane shear stresses were analyzed as well. An analogy between the dynamic analysis and corresponding quasistatic analysis implied that, in coated targets, it is likely that the shear stresses will produce subsurface damage such as debonding and striping of the coating.

References

[1] F.G. Hammitt, Cavitation and multiphase flow phenomena, McGraw-Hill, New York, 1980.
[2] M.B. Lesser, Thirty years of liquid impact research: a tutorial review, Wear 186 (1995) 28–34.
[3] F.P. Bowden, J.H. Brunton, The deformation of solids by liquid impact at supersonic speeds, Proc. R. Soc. London, Ser. A 263 (1961) 433–450.
[4] C. Westmark, G.W. Lawless, A discussion of rain erosion testing at the United States air force rain erosion test facility, Wear 186 (1995) 384–387.

[5] W.F. Adler, Particulate impact damage prediction, Wear 186 (1995) 35–44.

[6] F.P. Bowden, J.E. Field, The brittle fracture of solids by liquid impact, by solid impact, and by shock, Proc. R. Soc. London, Ser. A 282 (1964) 331–352.

[7] J.V. Hackworth, L.H. Kocher, I.C. Snell, Response of infrared transmitting materials to high-velocity impact by water drops, in: W.F. Adler (Ed.), Erosion: Prevention and Useful Applications, ASTM STP 664, American Society for Testing and Materials, Philadelphia, PA, 1979, pp. 255–278.

[8] D.G. Smith, R. Kinslow, Pressure due to high-velocity impact of a water jet, Exp. Mech. 18 (1976) 21–25.

[9] T. Obara, N.K. Bourne, J.E. Field, Liquid-jet impact on liquid and solid surfaces, Wear 186 (1995) 388–394.

[10] H.H. Shi, K. Takayama, N. Nagayasu, The measurement of impact pressure and solid surface response in liquid–solid impact up to hypersonic range, Wear 186 (1995) 352–359.

[11] J.E. Field, M.B. Lesser, J.P. Dear, Studies of two dimensional liquid-wedge impact and their relevance to liquid-drop impact problems, Proc. R. Soc. London, Ser. A 401 (1985) 225–249.

[12] J.P. Dear, J.E. Field, High-speed photography of surface geometry effects in liquid/solid impact, J. Appl. Phys. 63 (1988) 1015–1021.

[13] R.J. Hand, J.E. Field, D. Townsend, The use of liquid jets to simulate angled drop impact, J. Appl. Phys. 70 (1991) 7111–7118.

[14] S. Van der Zwaag, J.E. Field, Indentation and liquid impact studies on coated germanium, Philos. Mag. A 48 (1983) 767–777.

[15] M. Thomas, D. Price, M. Wilson, I. Perez, J.B. Boodey, W.R. Scott, R. Monro, A.B. Harker, Liquid jet impact measurements in diamond coated Ge substrates, in: Y. Tzeng, M. Yoshikawa, A. Murakawa, A. Feldman (Eds.), Applications of diamond films and related materials, Elsevier, New York, 1991, pp. 217–220.

[16] C.R. Seward, J.E. Field, E.J. Coad, Liquid impact erosion of bulk diamond, diamond composites and diamond coatings, J. Hard Mater. 5 (1994) 49–62.

[17] C.R. Seward, E.J. Coad, C.S.J. Pickles, J.E. Field, The liquid impact resistance of a range of IR-transparent materials, Wear 186 (1995) 375–383.

[18] O.G. Engel, Mechanism of high-speed-water-drop erosion of methyl methacrylate plastic, J. Res. Natl. Bur. Stand. 54 (1955) 51.

[19] F.J. Heymann, High-speed impact between a liquid drop and a solid surface, J. Appl. Phys. 40 (1969) 5113–5122.

[20] M.B. Lesser, Analytic solution of liquid-drop impact problems, Proc. R. Soc. London, Ser. A 377 (1981) 289–308.

[21] W.F. Adler, Liquid drop collisions on deformable media, J. Mater. Sci. 12 (1977) 1253–1271.

[22] J.E. Field, J.P. Dear, J.E. Ogren, The effect of target compliance on liquid drop impact, J. Appl. Phys. 65 (1989) 533–540.

[23] J.B. Hwang, F.G. Hammitt, High-speed impact between curved liquid surface and rigid flat surface, J. Fluids Eng. 99 (1977) 396–404.

[24] G.R. Johnson, Liquid–solid impact calculations with triangular elements, J. Fluids Eng. 99 (1977) 598–600.

[25] M. Rosenblatt, Y.M. Ito, G.E. Eggum, Analysis of brittle target fracture from a subsonic waterdrop impact. Erosion: Prevention and useful applications, in: W.F. Adler (Ed.), ASTM STP 664, American Society for Testing and Materials, Philadelphia, PA, 1979, pp. 227–254.

[26] R.M. Blowers, On the response of an elastic solid to droplet impact, J. Inst. Maths Applics 5 (1969) 167–193.

[27] A.G. Evans, On impact damage in the elastic response regime, J. Appl. Phys. 49 (1978) 3304–3310.

[28] A.G. Evans, Y.M. Ito, M. Rosenblatt, Impact damage thresholds in brittle materials impacted by water drops, J. Appl. Phys. 51 (1980) 2473–2482.

[29] S. van der Zwaag, J.E. Field, The effect of thin hard coatings on the hertzian stress field, Philos. Mag. A 46 (1982) 133–150.

[30] W.F. Adler, Waterdrop impact modeling, Wear 186 (1995) 341–351.

[31] W.F. Adler, D.J. Mihora, Analysis of waterdrop impacts on layered window constructions, SPIE 2286 (1994) 264–274.

[32] G. deBotton, Modeling the impact of waterdrops on targets with a thin protective layer, Comput. Modeling Simulation Eng. 2 (1997) 177–194.

[33] D.H. Kallas, Corrosion, wear, and erosion—an ancient art and a modern science, in: Erosion, wear, and interfaces with corrosion, ASTM STP 567, American Society for Testing and Materials, 1974, pp. 5–17.

[34] G. deBotton, Analysis of stresses and damage due to high-velocity waterdrop impact on coated targets, in: K.K. Panahi (Ed.), Proceedings of the 1997 ASME pressure vessels and piping conference, Vol. 355, 1997b, pp. 295–301.

[35] S.P. Timoshenko, J.N. Goodier, Theory of elasticity, McGraw-Hill, Singapore, 1970.

[36] H. Tada, P.C. Paris, G.R. Irwin, The stress analysis of cracks handbook, Del Research Corporation, 1973.

[37] I.S. Raju, J.C. Newman, Stress intensity factors for a wide range of semi-elliptical surface cracks in finite-thickness plates, Eng. Fract. Mech. 11 (1979) 817–829.